

Resonant Generation of Internal Waves on a Model Continental Slope

H. P. Zhang, B. King, and Harry L. Swinney

Center for Nonlinear Dynamics and Department of Physics, The University of Texas at Austin, Austin, Texas 78712, USA

(Received 5 February 2008; published 20 June 2008)

We study internal wave generation in a laboratory model of oscillating tidal flow on a continental margin. Waves are found to be generated only in a near-critical region where the slope of the bottom topography matches that of internal waves. Fluid motion with a velocity an order of magnitude larger than that of the forcing occurs within a thin boundary layer above the bottom surface. The resonant wave is unstable because of strong shear; Kelvin-Helmholtz billows precede wave breaking. This work provides a new explanation for the intense boundary flows on continental slopes.

DOI: [10.1103/PhysRevLett.100.244504](https://doi.org/10.1103/PhysRevLett.100.244504)

PACS numbers: 47.35.Bb, 47.20.Ft, 91.50.Bd

Introduction.—Away from shallow, well-mixed surface regions, the density of sea water increases with depth due to variation in salinity and temperature [1]. Under the influence of gravity, this density stratification provides the restoring force for a class of waves *within* the ocean interior called internal waves. In a nonrotating stratified fluid (Coriolis parameter $f = 0$), internal waves with frequency ω propagate with a slope (tangent of the angle between the group velocity direction and the horizontal) determined by the dispersion relation [2]:

$$S_w = \sqrt{\frac{\omega^2}{N^2 - \omega^2}}, \quad (1)$$

where $N = \sqrt{-(g/\rho_0)(\partial\rho/\partial z)}$ is the local buoyancy frequency. This unusual dispersion relation leads to many counterintuitive dynamical phenomena, such as critical reflection [3] and wave attractors [4].

A significant fraction of the internal waves in the oceans are generated by *oscillatory* tides flowing over ocean topography such as continental margins and underwater mountains [5]. This can be appreciated in a reference frame moving with the tides; an ocean boundary then acts like an oscillating wavemaker. The particular case of wave generation from continental margins has been studied both theoretically [6,7] and experimentally [8,9] because internal waves affect many coastal processes [10–14].

As in previous work [6–9], we consider a two-dimensional model topography for continental margins, which consists of two horizontal segments connected by a slanted segment, as shown in Fig. 1(a). The slanted segment mimics a steep continental slope and has topographic slope $S_t = \Delta z/\Delta x$. The horizontal segments mimic the less steep continental rise and shelf, and the arc connecting the upper horizontal segment with the sloping segment represents the shelf break.

An important fluid dynamical parameter in the problem is the ratio S_w/S_t . Recent oceanic observations have revealed many locations where the angle of the continental slope is close to that of local semidiurnal internal waves (approximately a 12-hour period); thus, the regime $S_w \sim S_t$

occurs frequently [10]. However, neither previous experiment nor theory provides a clear physical picture for wave generation in this regime. The experimental studies [8,9] have focused on regimes of $S_w < S_t$ and $S_w > S_t$, while theory has considered inviscid fluids and predicts divergent velocity fields for $S_w = S_t$ [6,7]. We present here an investigation of this important yet unexplored parameter regime. Our work also provides insight into the general problem of tidally driven internal wave generation by topography.

Experiment.—Experiments are performed in a glass tank (95 cm long, 45 cm thick, and 60 cm high) filled with a linearly stratified salt solution with buoyancy frequency $N = 1.55$ rad/s. A two-dimensional model topography immersed in the tank [see Fig. 1(a)] has a slope and length that can be varied; two topographies used in the present work have the same slope $S_t = 0.73$ (corresponding to a 36° angle) but different lengths $L = 5.5$ cm and $L = 18.4$ cm. The dimension perpendicular to the paper is $W = 25$ cm, sufficiently wide to yield two-dimensional flow away from the edges.

Particle image velocimetry (PIV) is used to measure the velocity field in a vertical plane. A laser light sheet (1 W and 0.5 mm thick) illuminates fluid that is uniformly seeded with TiO_2 particles (~ 1 – 10 micrometers). Images obtained with a resolution of 1004×1004 pixels are analyzed by using an image correlation algorithm [15]. The velocity field is obtained on a 100×100 grid with an rms error less than 5% over an area of 15×15 cm². Fluid density is measured with a conductivity probe (Precision Measurement Engineering); the conductivity probe and a thermometer are mounted on a translation stage. Fluorescent dye (Rhodamine 6G) is used to visualize material transport and mixing.

To simulate oscillatory tidal flow, the topography is oscillated sinusoidally in the horizontal direction with amplitude A and frequency ω ; A and ω are experimental analogs of the tidal excursion distance and tidal forcing frequency, respectively. The maximum forcing velocity is $V_f = A\omega$. To mimic oceanic conditions, A is made small compared to the size of the topography, and $A = 0.1$ cm is

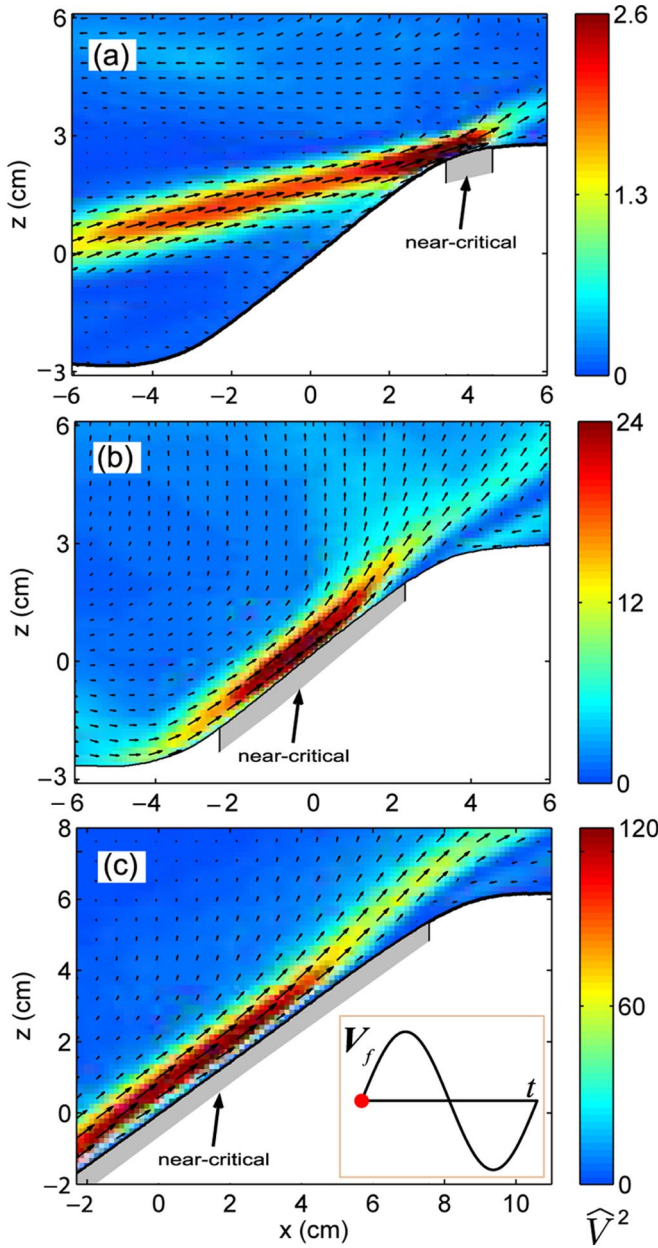


FIG. 1 (color online). The horizontally oscillating topography generates (a) a nonresonant internal wave when the wave slope differs from the topographic slope (here $S_w = 0.51 S_t$) and (b) a resonant wave when the slopes are equal; the oscillation frequency is 0.46 rad/s in (a) and 0.91 rad/s in (b). A stronger resonant wave forms in (c), where the wave and topographic slopes match for a larger distance—the near-critical region lengths are 5.9 and 19.5 cm in (b) and (c), respectively (other parameters are the same). The arrows are instantaneous velocity vectors. The color represents the normalized kinetic energy density in the wave $|\hat{V}(\vec{r}, t)|^2 \equiv |\vec{V}(\vec{r}, t)/V_f|^2$; the color bar scales are *different* for each panel. The phase of tidal forcing for all cases is shown in the inset in (c). In (c), the imaging window covers only the top part of the topography. Gravity is the $-\hat{z}$ direction. Gray shading indicates the region of near-critical topography (see text).

used throughout the Letter except for data in Fig. 4(b). The velocity measurements are made in the laboratory reference frame and are transformed to the frame of the oscillating topography to facilitate interpretation.

Results.—Nonresonant and resonant waves generated by tidal motion are illustrated in Figs. 1(a) and 1(b), respectively. Since a fluid particle in an internal wave field moves in the direction of wave propagation, the boundary condition $\vec{V} \cdot \hat{n} = 0$ (\hat{n} denotes the normal direction) can be satisfied *only* where the local topographic slope matches the wave slope: $S_t(\vec{r}) \sim S_w$ [8,9,16,17]. We define the “near-critical” region to be where $|S_t(\vec{r}) - S_w| < 0.09$; this region is indicated by gray shading in Fig. 1.

Waves are generated only in a near-critical region. In the off-resonant case [Fig. 1(a)], the length of the near-critical region is small, and the generated wave is weak. At resonance, the wave is generated over the *whole* region of constant slope and superposes to make a strong wave. The wave strength increases with the increasing length of the critical region [cf. Eq. (4)]. For example, the near-critical region in Fig. 1(c) is 3.3 times as long as in Fig. 1(b), and the resultant maximum kinetic energy density is 5 times as large.

The flow strength exhibits a strong maximum at the forcing frequency that satisfies the resonant condition $S_t = \sqrt{\omega_f^2/(N^2 - \omega_f^2)}$, as shown in Fig. 2. The half-width of the resonance is $\Delta\omega = 0.05$ rad/s. By combining this with (1) and $\omega = 0.91$ rad/s, we get $\Delta S = |S_t - S_w| = 0.06$, which means that a resonant wave is generated in the

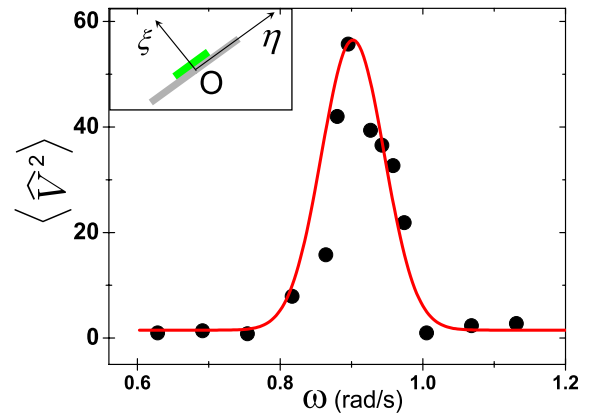


FIG. 2 (color online). Flow strength, measured over the long slope [Fig. 1(c)] as a function of the forcing frequency, is sharply peaked at the resonant frequency where $S_w = S_t$; the red line is a guide to the eye. The flow strength is represented by the normalized kinetic energy density averaged for two oscillation periods for the region in the green box region in the inset ($-3.1 \text{ cm} < \eta < 2.66 \text{ cm}$ and $0 < \xi < 1 \text{ cm}$), where η and ξ are axes parallel and perpendicular to the boundary, respectively. We note that $\langle \hat{V}^2 \rangle$ is a local measurement of kinetic energy in baroclinic motion; this differs from the energy conversion rate (see [5]), which is the globally integrated energy change from barotropic to baroclinic motion.

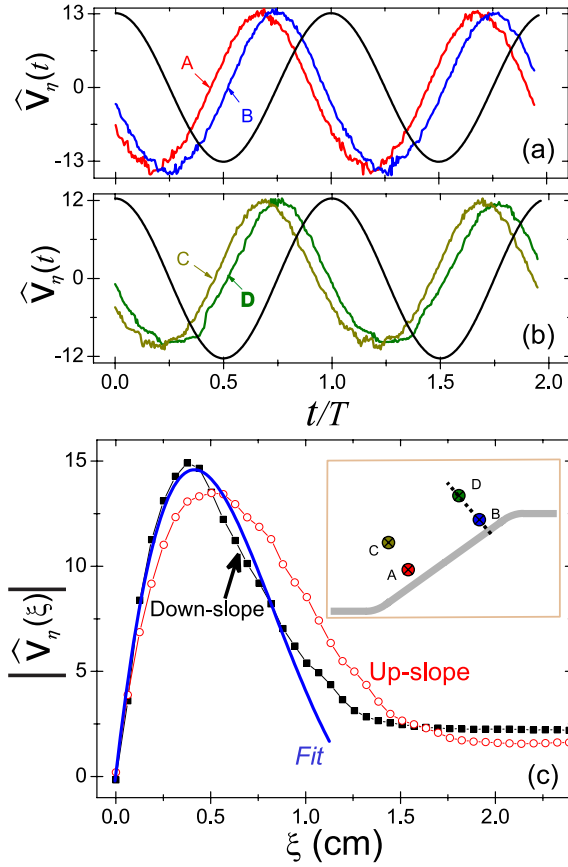


FIG. 3 (color online). Spatiotemporal characteristics of the resonantly generated wave measured over the large topography [Fig. 1(c)]. (a),(b) Time series of the normalized along-slope velocity component at locations (η, ξ) shown in the inset in (c): $A = (-2.27, 0.38)$, $B = (1.99, 0.38)$, $C = (-2.27, 0.69)$, and $D = (1.99, 0.69)$, in units of centimeters. The phase of the forcing is shown by black lines for reference. Time is normalized by the forcing period. (c) Profile of $|\hat{V}_\eta(\xi)|$ for maximum upslope and downslope flow through the line through B and D . The blue line is generated from Eq. (2) with the experimentally determined $a = 0.34$ cm, $k\eta - \omega t = 0$, and $V_m = 14.7$.

region $0.91 < S_w/S_t < 1.09$ (where $S_t = 0.73$). Other representations of the flow strength such as averaged shear stress on the topography have been tested and yield similar resonant behavior.

A resonantly generated internal wave has nontrivial spatial and temporal properties [18], as Fig. 3 illustrates. The phase of the forcing velocity and the normalized velocity component along the slope $\hat{V}_\eta(\vec{r}, t) = V_\eta(\vec{r}, t)/V_f$ are plotted in Figs. 3(a) and 3(b) for four points. The velocity fields are periodic with the forcing period T and are approximately a $\pi/2$ phase behind the forcing. There is a phase variation $\Delta\phi(\eta)$ along the slope (e.g., between points A and B) and a very small phase difference for displacements perpendicular to the slope; $\Delta\phi(\eta)$ depends linearly on η , $\Delta\phi(\eta) = k\eta$, where $k = 0.1$ rad/cm for $\Delta\phi$ in radians and η in centimeters. Measurements with different slope lengths L indicate that $k \approx 2/L$. The varia-

tion of the velocity amplitude along the constant topographic slope is small. The flow is temporally periodic, but the downslope flow is somewhat stronger and thinner than the upslope flow, as the profiles of $|\hat{V}_\eta(\xi)|$ plotted in Fig. 3(c) show. For points close to the boundary (e.g., points A and B), the downslope flow is stronger than the upslope flow by about 10%; the reverse is true for points C and D .

The fluid motion is confined to a thin boundary layer, as shown in Fig. 3(c), where the layer thickness (HWHM) is 0.38 cm, 3 times that of a Stokes layer, whose thickness would be $\sqrt{2\nu/\omega} = 0.13$ cm (ν is the kinematic viscosity). For a flow field sinusoidal in time and two-dimensional in space, the linearized dynamical equations can be simplified under the ‘‘boundary layer’’ approximation [19,20], which assumes that the variation is much stronger across the slope than along the slope, i.e., $\partial_\xi \gg \partial_\eta$. In the boundary layer, the simplified equation can be written as $\partial_\eta(V_\eta) = i(\nu/2\sqrt{N^2 - \omega^2})\partial_{\xi\xi\xi}(V_\eta)$, which has the solution [20]

$$V_\eta(\xi, \eta, t) = \frac{V_m}{0.47} e^{-(\xi/2a)} \sin\left(\frac{\sqrt{3}}{2} \frac{\xi}{a}\right) \cos(k\eta - \omega t), \quad (2)$$

where

$$a = \left(\frac{\nu}{2k\sqrt{N^2 - \omega^2}}\right)^{1/3} \approx \left(\frac{\nu L}{4\sqrt{N^2 - \omega^2}}\right)^{1/3} \quad (3)$$

is the length scale in the $\hat{\xi}$ direction and $a = 0.34$ cm for $L = 18.5$ cm. An expression for the maximal velocity V_m can be found by the following consideration. As the topography oscillates, material is transported from one side of the shelf break to the other. From the motion of the boundary, the maximal instantaneous material flux can be estimated as $F = V_f W L \sin\theta = V_f W L \frac{\omega}{N}$. At resonance, the flow field is dominated by the boundary flow, and an estimate of the maximal material flux is given by integrating across the boundary flow from $\xi = 0$ to $\xi = 3.5a$: $F = V_f W \int_0^{3.5a} \frac{V_m}{0.47} e^{-(\xi/2a)} \sin\left(\frac{\sqrt{3}}{2} \frac{\xi}{a}\right) d\xi = V_f \frac{V_m}{0.47} a W$. By equating the two expressions for flux and using (3), we obtain a scaling relation for the dependence of the maximum velocity on the length L of a near-critical region:

$$V_m = 0.75 \frac{\omega}{N} \left(\frac{\sqrt{N^2 - \omega^2}}{\nu}\right)^{1/3} L^{2/3}. \quad (4)$$

The velocity profile predicted by (2) using parameters calculated from (3) and (4) is in good accord with measurements in the boundary layer ($\xi < 1$ cm) [see Fig. 3(c)]. Further, in typical ocean conditions where a semidiurnal wave ($\omega = 1.45 \times 10^{-4}$ rad/s) is generated at a continental slope at angle $\theta = 2^\circ$ ($\omega/N = 0.035$), we obtain $V_m = 14.4$ for $L = 200$ m. This large effect for a constant topographic slope only 200 m long indicates that the resonant waves should be important in many places in the oceans.

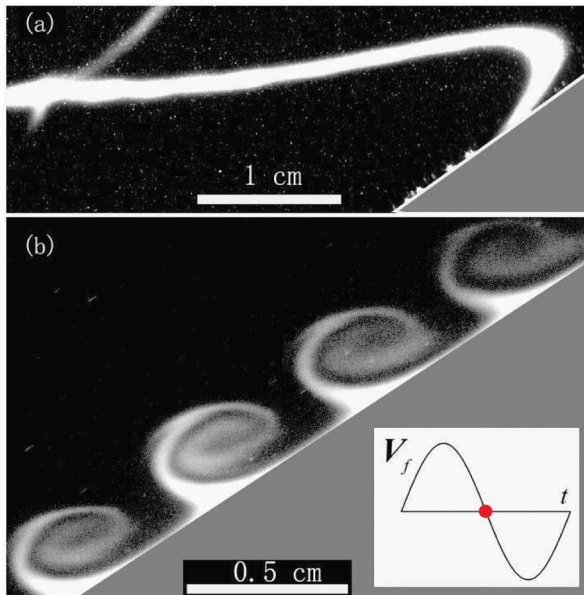


FIG. 4 (color online). (a) Distortion of an isopycnal line by resonant wave near the boundary ($A = 0.1$ cm). The flow is visualized by using fluorescent dye illuminated by a vertical light sheet; the dye was deposited in a horizontal layer before the experiment. (b) Kelvin-Helmholtz billows form for $A = 0.4$ cm. This flow is visualized by laying a thin layer of dye along the slope before the experiment. The phase of forcing is shown in the inset in (b); the phase for (a) is $\pi/2$ ahead.

The resonantly generated internal wave causes strong shear above the topography because of the large velocity and small length scale. The strong shear causes an inversion in the density gradient even with weak forcing (e.g., $A = 0.1$ cm), as shown by a snapshot of a dye line in Fig. 4(a). The overturning happens only in a small region $\xi < 0.4$ cm, which leads to a small Rayleigh number and hence a small growth rate for convective instability. The flow then reverses, and the isopycnals stabilize before the perturbations grow to large amplitude; hence, the flow remains laminar, and no wave breaking or mixing is observed. This is consistent with Thorpe's analysis and experiments on standing waves [21].

Increasing the forcing amplitude leads to a linear increase of fluid velocity up to about $A = 0.4$ cm, while the thickness of the boundary layer remains approximately unchanged. Then the time-averaged Richardson number is low enough, $\langle \text{Ri} \rangle_t = \langle N^2 / (dV/dz)^2 \rangle_t \approx 0.08$, for shear instability, and Kelvin-Helmholtz billows form, as illustrated in Fig. 4(b). These billows eventually break and cause mixing.

Conclusion.—Our experiments have shown that strong resonant internal waves are generated by periodic tidal-like flows over a long topographic slope which has an angle close to the internal wave propagation angle (i.e., $S_t \approx S_w$). The maximal boundary layer velocity increases as $L^{2/3}$, where L is the length of the near-critical region; this result needs to be taken into account in theoretical

models [5]. The resonant flow is confined to a region about 3 times as thick as the Stokes boundary layer; downslope flow is slightly faster and thinner than upslope flow. The strong shear perpendicular to the slope leads to density inversion and the formation of Kelvin-Helmholtz billows.

This work provides a new explanation of the intense boundary flows observed on continental slopes when $S_t \approx S_w$ [10,14,22]. The conventional explanation is that such flows are created by critical reflection of remotely generated internal waves [10,14]. The intense boundary currents strongly affect material transport by sustaining turbidity currents [13] and generating nepheloid layers (particle-rich layers above the ocean floor) [11,12]. These strong currents also play a role in shaping the continental slopes [10].

We thank William R. Young for suggesting Eq. (2). This research was supported in part by the Sid W. Richardson Foundation.

- [1] C. Wunsch and R. Ferrari, *Annu. Rev. Fluid Mech.* **36**, 281 (2004).
- [2] P. K. Kundu and I. M. Cohen, *Fluid Mechanics* (Elsevier, New York, 2004).
- [3] C. Wunsch, *J. Fluid Mech.* **35**, 131 (1969).
- [4] L. R. M. Maas, D. Benielli, J. Sommeria, and F. P. A. Lam, *Nature (London)* **388**, 557 (1997).
- [5] C. Garrett and E. Kunze, *Annu. Rev. Fluid Mech.* **39**, 57 (2007).
- [6] P. G. Baines, *Deep-Sea Res. A* **29**, 307 (1982).
- [7] P. D. Craig, *J. Mar. Res.* **45**, 83 (1987).
- [8] P. G. Baines and F. Xinhua, *Dyn. Atmos. Oceans* **9**, 297 (1985).
- [9] L. Gostiaux and T. Dauxois, *Phys. Fluids* **19**, 028102 (2007).
- [10] D. A. Cacchione, L. F. Pratson, and A. S. Ogston, *Science* **296**, 724 (2002).
- [11] P. Puig, A. Palanques, J. Guillen, and M. El Khatab, *J. Geophys. Res. Oceans* **109**, C09011 (2004).
- [12] E. McPhee-Shaw, *Deep-Sea Res. II* **53**, 42 (2006).
- [13] H. Toniolo, M. Lamb, and G. Parker, *J. Sediment. Res.* **76**, 783 (2006).
- [14] J. D. Nash, E. Kunze, J. M. Toole, and R. W. Schmitt, *J. Phys. Oceanogr.* **34**, 1117 (2004).
- [15] A. Fincham and G. Delerce, *Exp. Fluids* **29**, S13 (2000).
- [16] H. P. Zhang, B. King, and H. L. Swinney, *Phys. Fluids* **19**, 096602 (2007).
- [17] T. Peacock, P. Echeverri, and N. Balmforth, *J. Phys. Oceanogr.* **38**, 235 (2008).
- [18] See EPAPS Document No. E-PRLTAO-101-034852 for movies of tracer particles, PIV results, and dye visualization. For more information on EPAPS, see <http://www.aip.org/pubservs/epaps.html>.
- [19] D. G. Hurley and G. Keady, *J. Fluid Mech.* **351**, 119 (1997).
- [20] T. Dauxois and W. R. Young, *J. Fluid Mech.* **390**, 271 (1999).
- [21] S. A. Thorpe, *J. Fluid Mech.* **260**, 333 (1994).
- [22] M. D. Levine and T. J. Boyd, *J. Phys. Oceanogr.* **36**, 1184 (2006).